Wafer-scale development, characterization, and high temperature stabilization of epitaxial Cr₂O₃ films grown on Ru(0001) ⊘

Quintin Cumston; Matthew Patrick ⁽¹⁾; Ahmed R. Hegazy ⁽¹⁾; Amirali Zangiabadi ⁽¹⁾; Maximillian Daughtry; Kevin R. Coffey ⁽¹⁾; Katayun Barmak ⁽¹⁾; William E. Kaden [™] ⁽¹⁾



J. Chem. Phys. 160, 144705 (2024)

https://doi.org/10.1063/5.0201818





Articles You May Be Interested In

Promoting effect of CO₂ on NiCr oxidation: Atomistic origins based on first principles

J. Chem. Phys. (October 2024)

Cr₂O₃ layer inhibits agglomeration of phosphine-protected Au₉ clusters on TiO₂ films

J. Chem. Phys. (October 2021)

Increasing the Néel temperature of magnetoelectric chromia for voltage-controlled spintronics

Appl. Phys. Lett. (June 2014)



The Journal of Chemical Physics

Special Topics Open for Submissions

Learn More



Wafer-scale development, characterization, and high temperature stabilization of epitaxial Cr₂O₃ films grown on Ru(0001)

Cite as: J. Chem. Phys. 160, 144705 (2024); doi: 10.1063/5.0201818 Submitted: 31 January 2024 • Accepted: 19 March 2024 • **Published Online: 9 April 2024**







Quintin Cumston,¹ Matthew Patrick,² D Ahmed R. Hegazy,³ D Amirali Zangiabadi,² Maximillian Daughtry,³ Kevin R. Coffey, 6 Katayun Barmak, 2 and William E. Kaden 3.a)

AFFILIATIONS

- Department of Electrical and Computer Engineering, University of Central Florida, 4328 Scorpius Street, Orlando, Florida 32816, USA
- ² Department of Applied Physics and Applied Mathematics, Columbia University, 500 W. 120th Street, New York, New York 10027, USA
- Department of Physics, University of Central Florida, 4111 Libra Drive, Orlando, Florida 32816, USA
- 4 Department of Materials Science and Engineering, University of Central Florida, 12760 Pegasus Drive, Orlando,
- a) Author to whom correspondence should be addressed: william.kaden@ucf.edu

ABSTRACT

This work outlines conditions suitable for the heteroepitaxial growth of Cr₂O₃(0001) films (1.5-20 nm thick) on a Ru(0001)-terminated substrate. Optimized growth is achieved by sputter deposition of Cr within a 4 mTorr Ar/O₂ 20% ambient at Ru temperatures ranging from 450 to 600 °C. The Cr₂O₃ film adopts a 30° rotated honeycomb configuration with respect to the underlying Ru(0001) substrate and exhibits a hexagonal lattice parameter consistent with that for bulk Cr₂O₃(0001). Heating to 700 °C within the same environment during film preparation leads to Ru oxidation. Exposure to temperatures at or above 400 °C in a vacuum, Ar, or Ar/H2 3% leads to chromia film degradation characterized by increased Ru 3d XPS intensity coupled with concomitant Cr 2p and O 1s peak attenuations when compared to data collected from unannealed films. An ill-defined but hexagonally well-ordered Rux CryOz surface structure is noted after heating the film in this manner. Heating within a wet Ar/H $_2$ 3% environment preserves the Cr $_2$ O $_3$ (0001)/Ru(0001) heterolayer structure to temperatures of at least 950 °C. Heating an Ru-Cr₂O₃-Ru heterostacked film to 950 °C within this environment is shown by cross-sectional scanning/transmission electron microscopy (S/TEM) to provide clear evidence of retained epitaxial bicrystalline oxide interlayer structure, interlayer immiscibility, and epitaxial registry between the top and bottom Ru layers. Subtle effects marked by O enrichment and O 1s and Cr 2p shifts to increased binding energies are noted by XPS in the near-Ru regions of Cr₂O₃(0001)/Ru(0001) and Ru(0001)/Cr₂O₃(0001)/Ru(0001) films after annealing to different temperatures in different sets of environmental conditions.

Published under an exclusive license by AIP Publishing. https://doi.org/10.1063/5.0201818

I. INTRODUCTION

Cr2O3 has received considerable scientific interest for its applications in chemical catalysis, 1,2 gas sensing,3 corrosion resistance,4 and as an insulating magnetic material.5 The oxide adopts a corundum crystal structure described by a trigonal (R3c) unit cell (a = 5.35 Å; $\alpha = 55.00^{\circ}$) often expressed using conventional hexagonal lattice parameters (a = 4.9407 Å, c = 13.5783 Å; $\alpha = 90^{\circ}$, $\gamma = 120^{\circ}$). Due to its use as a high-temperature corrosion

mitigation coating, many investigations of oxide decomposition, volatilization, and support interactions have been reported as a function of temperature under varied atmospheric conditions.^{17–22} Unsupported and bulk Cr₂O₃ passivation scales are known to be generally stable below 1000 °C, after which sub-Å/min decomposition and volatilization occur at different rates depending on the composition of the gas phase environment (O2containing steam environments proving most detrimental).¹⁷⁻²¹ Therefore, differences in corrosion resistance are primarily dependent on the material properties of the Cr_2O_3 /alloy interface. For example, interstitial diffusion between Cr_2O_3 and Zircaloy-4 alloyed fuel rod cladding (Zry4) is known to create brittle $ZrCr_2$ interlayers at elevated temperatures ($T=900\,^{\circ}C$) that weaken the corrosion resistant performance of the oxide passivation layer. Oxide—metal interactions are also known to influence the catalytic properties of active sites present at the surface of solid-state heterogeneous catalysts, with synergistic $Cu-Cr_2O_3$ interactions shown to promote Cu activity toward the water gas shift reaction catalyzed by Cr_2O_3/Cu inverse catalyst structures.

The creation of well-defined surface terminations is often needed to enable fundamental studies of various structure-property relationships important to the design of new materials. Previous approaches used to produce structurally controlled chromium oxide interfaces include the oxidation of low index Cr singlecrystals, $^{28-41}$ the preparation of α -Cr₂O₃(0001) from bulk single-crystals, $^{42-44}$ and the heteroepitaxial growth of oxide thin films templated by select sets of metal single-crystal substrates.^{2,45-3} Among the latter approaches, Pt(111), 45,51 Pd(111), 1,2 Ag(111), 46 Cu(111),⁴⁷ and Co(0001)⁵² are reported to cause template growth of (0001)-terminated Cr₂O₃ thin films due, in part, to favorable lattice mismatch characteristics. For example, $\sqrt{3} \times \sqrt{3} R30^{\circ} Cr_2 O_3/M$ superstructures expressed relative to the (111) terminations of Pt, Pd, and Ag exhibit ~1% to 5% mismatch with respect to the bulk Cr₂O₃(0001) lattice. The same superstructure produced on Ru(0001) (a = 2.7059)⁵³ would present a comparable ~6% compressive mismatch with respect to the unsupported Cr₂O₃(0001) lattice. Relative to the same subset of metals, ruthenium exhibits intermediate electron affinity and a significantly higher melting point, indicating a likelihood for similar surface chemistry characteristics and increased amenability to high temperature investigation. Given these characteristics, this work investigates Ru(0001)'s viability as an alternative substrate, allowing for the growth of (0001) terminated Cr₂O₃ thin-films suitable for further exploration of metal-dependent, oxide-support interactions.

The authors' explicit interest in this specific combination of materials stems from ongoing work dedicated to the fabrication of geometrically controlled, single-crystalline Ru nanowires relevant to improved performance in metallic interconnects central to overall CMOS performance characteristics. ⁵⁴ Fabrication of single-crystalline nanowires eliminates otherwise deleterious grain-boundary contributions to wire resistivity. Exploration of crystallographically anisotropic transport effects requires the creation of nanowires both parallel and perpendicular to the wafer surface plane. Meeting the latter challenge requires the development of an epitaxial dielectric interlayer that retains a registry with an underlying Ru electrode for dielectric films of varied thickness when heated to temperatures requisite for Ru crystallization. Therefore, particular emphasis is placed on both the thickness and temperature dependencies of the reported film characteristics.

II. EXPERIMENTAL METHODS

A. Sample preparation

2-in. diameter α -Al₂O₃(0001) sapphire wafers (MTI) were preconditioned by heating in a tube furnace within the air at 1000 $^{\circ}$ C for

30 min to remove adsorbed surface contaminants immediately prior to insertion into the deposition chamber. All depositions were completed within an ATC2200 UHV sputtering system obtained from AJA International Inc. (base pressure $\approx 1 \times 10^{-8}$ Torr). Ru(0001) films were deposited from a 2-in. diameter Ru (99.95%) target via DC magnetron sputtering within a 4 mTorr Ar/H₂ 3% ambient while maintaining a constant 700 °C sapphire wafer temperature using a quartz halogen radiant heating lamp.⁵⁴ The x-ray reflectivity (XRR) calibrated deposition rate was found to be 0.13 nm/s when operating the magnetron source at 200 W, and deposition time was varied to create films of desired thicknesses ranging from 20 to 160 nm. Wafers were subsequently cooled to specified Cr deposition temperatures within the Ar/H₂ ambient before replacing the gas with either 4 mTorr Ar/H₂ 3% or Ar/O₂ 20% to establish conditions suitable for the production of either Cr or CrO_x films. Cr was then deposited from a 2-in. Cr target (99.95%) by 200 W DC sputtering at XRR-calibrated rates of 6.75 and 6.42 nm/min for the deposition of either Cr or CrO_x, respectively, to produce films ranging from 1.5 to 20 nm in thickness. Select films were subsequently covered with 20 nm Ru at 300 °C within 4 mTorr Ar using the aforementioned Ru magnetron conditions and/or rapidly heated to specified temperatures for ~1 min within either high vacuum $(\sim 1 \times 10^{-8} \text{ Torr})$, 4 mTorr Ar/O₂ 20%, or 1 atm of flowing wet Ar/H₂ 3%. Post deposition annealing steps were completed both in situ and ex situ within a near-ambient pressure x-ray photoelectron spectroscopy (NAP-XPS) chamber or a tube furnace. The wet Ar/H₂ 3% annealing cycles were completed exclusively within the tube furnace by bubbling the gas composition through water prior to allowing the mixture to flow into a freely exhausted heated quartz tube. Prior to ex situ analysis or post processing, wafers were scribed and cleaved into \sim 7 × 7 mm² pieces to accommodate spatial limitations specific to several additional pieces of equipment. One sample created by 950 °C wet Ar/H₂ annealing wafer segments prepared by sequential deposition of 20 nm Ru at 700 °C within Ar/H₂ 3%, 20 nm CrO_x at 600 °C within Ar/O₂ 20%, and 20 nm Ru at 300 °C within Ar was subsequently encapsulated with a thin (~5 nm) protective Al layer in preparation for additional cross-sectional scanning/transmission electron microscopy (S/TEM) characterization. Electron transparent cross sections amenable to S/TEM characterization were prepared by focused ion beam (FIB) milling in an FEI Helios NanoLab 660 dual beam instrument. The direction normal to the prepared cross section was parallel to $[11\overline{2}0]$ in sapphire and, thus, parallel to $[10\overline{1}0]$ in the epitaxially deposited Ru layer. A carbon containing layer was manually applied to the sample prior to the FIB milling to allow for ready identification of the deposited aluminum layer.

B. Sample characterization

Samples were characterized by XRR, x-ray diffraction (XRD), XPS, low energy electron diffraction (LEED), and S/TEM. XRD and XRR were performed using a Panalytical X'pert3 MRD system equipped with a copper source, a graded multilayer mirror used to create the incident beam, and a 1D PIXcel detector used to monitor the intensity of the diffracted beam. Both XRD and XRR employed identical optical configurations. Layer thicknesses were extracted from XRR fits produced by slab models created within the Panalytical X'pert reflectivity software suite. Input slabs consisted of Cr₂O₃,

RuO, Ru, and sapphire using respective density values of 5.134, 6.273, 13.1, and 3.59 g/cm³.

LEED and XPS were conducted within a separate ultrahigh vacuum system ($\sim 1 \times 10^{-10}$ Torr) equipped with a 6-in. backview LEED apparatus (OCI, Microengineering) and a SPECS XPS electron spectrometer consisting of an XR 50 Al Ka source and a PHOIBOS 100 hemispherical energy analyzer. The azimuthal surface orientation was uncontrolled when mounting different samples for LEED analysis, and electron beam energies of 77 and 100 eV were used as needed to allow for clear separation of individual diffraction reflexes. All samples were grounded via Ta front contacts used to secure individual samples to exchangeable metallic sample holding plates at the periphery of the cleaved wafer segments. Separate in situ XPS characterization of select samples was completed as a function of temperature (25-600 °C) within 0.8 mTorr O2 using a ScientaOmicron HiPP Lab AP XPS system equipped with a monochromated Al Ka source and a differentially pumped HiPP-3 electron energy analyzer. Sample holders were exchangeable with those used in the UHV system, and heating was controlled using a radiant resistive heater mounted behind the sample holder. All XPS measurements (in both systems) were completed using fixed source-sample-analyzer geometries separating the source and detection axes by 55° with electrons collected along the surface

Energy dispersive x-ray spectroscopy (EDS) and S/TEM characterization of the electron transparent cross sections were conducted on a ThermoFisher/FEI Talos F200X instrument. The instrument was operated at 200 kV.

III. RESULTS AND DISCUSSION

A. Chromia growth and characterization

A literature review of both epitaxial and non-epitaxial α-Cr₂O₃ film growth suggests preferable conditions for crystal formation above 500 K when depositing Cr within mTorr Ar/O_2 15%–20%, $^{1,2,45-47,51,52,55,56}$ with further increases in substrate temperature leading to modest increases in O:Cr stoichiometry without causing significant changes in crystal structure.⁵⁶ Many of the epitaxial films form unique (often metastable) superstructures at near monolayer equivalent chromia coverages, with most exhibiting a preference for Cr₂O₃(0001) when increasing coverage and/or deposition/oxidation temperature. 1,2,45,46,51,52,55 Furthermore, both reactive deposition of Cr within O2 environments and sequential cycles of Cr deposition and subsequent oxidation have proven viable for epitaxial film growth.

Based on the previous review of pertinent literature, an initial film (film 1) was prepared by depositing ~0.8 nm Cr onto a [sapphire(0001)-supported] 160 nm Ru(0001) film within Ar before switching to Ar/O₂ 20% while maintaining a 350 °C wafer temperature throughout the duration of the full process to produce a ~10 nm thick CrO_x layer. To ensure complete oxidation, the wafer was subsequently heated to 700 °C (and allowed to cool) within the Ar/O₂ environment. After reestablishing room temperature, the wafer was extracted and cleaved for characterization. Cr 2p and O 1s XPS obtained from this film are provided in the lower portion in Fig. 1(a). The complete absence of detectable Ru 3d (not shown) is consistent with the formation of a fully wetted chromia film. Quantitative comparison of the O 1s and Cr 2p peaks yields an integrated O 1s:Cr 2p intensity ratio of 0.43:1, which suggests an O:Cr stoichiometry of ~1.43:1 when applying reference O 1s and Cr 2p atomic sensitivity factor corrections, in reasonable agreement with the anticipated formation of Cr₂O₃.⁵⁷ Qualitative interpretations of chemical-states using peak locations are complicated by differences in oxide charging, surface dipoles created at the metal interface, and substrate work-functions after exposure to different film growth conditions on different substrates. 58,59 As a result, there are significant discrepancies in the literature when reporting Cr 2p and O 1s binding energies attributed to Cr₂O₃, which span ranges of 575.5-576.9 and 529.6-530.9~eV for Cr $2p_{3/2}$ and O 1s, respectively. 1,46,50,52,55 Our value ues for Cr 2p_{3/2} (576.3 eV) and O 1s (530.0 eV) fall within these ranges and are taken to provide reasonable internal reference values indicative of the presence of fully oxidized Cr₂O₃/Ru thin-films.

A second 1.5 nm thick CrO_x film (film 2) was grown on a separate 160 nm Ru(0001)/Al $_2$ O $_3$ (0001) wafer by sputtering \sim 0.8 nm Cr onto the surface at 350 °C within Ar and subsequently annealing to 700 °C within an Ar/O2 20% ambient. The Cr 2p, O 1s, and Ru 3d spectra collected from this sample are provided in the upper portion in Fig. 1(a). Notably, the Cr 2p and O 1s peak positions and line shapes are nearly identical to those obtained from the thicker internal reference. From this, we might infer a similar, if not identical, chemical-state indicative of Cr₂O₃. Unlike the thicker film, this film is now thin enough to detect underlying Ru 3d signal intensity. In this case, the peak has been fitted with two components, denoting the positions associated with metallic Ru⁰ (blue) and RuO2 (red) constituents. The metallic line shape and position have been empirically established using data collected from a silica-capped Ru film step-annealed to 500 °C within Ar/H₂ 3% [see Refs. 54 and 60] and include minor contributions expected from adventitious carbon resulting from air exposure when exchanging between chambers. All Ru 3d spectra were first fit with this highly constrained peak, and additional components were only added as needed. In this case, the spectrum required the dominant presence of a broad peak centered at Ru $3d_{5/2} = 280.8$ eV, which is consistent with the formation of RuO₂.⁵⁷ Accordingly, a 529.4 eV component was included when fitting the O 1s spectrum to reflect the presence of RuO₂.⁵⁷ The O 1s spectrum was fit using a positionally unconstrained peak bound to an upper limit integrated intensity reflective of fully oxidized Cr_2O_3 ($I=0.45I_{Cr_{2p}}$), and the intensity of the positionally constrained RuO₂ feature was then allowed to grow as needed to satisfactorily fit the data. All data are consistent with the formation of fully oxidized Cr₂O₃ present on heavily oxidized RuO2/Ru.

Despite clear evidence of RuO₂ formation, a LEED pattern was collected from the second film [Fig. 1(b)] and indicates the formation of a superstructure symmetrically consistent with a $\sqrt{3} \times \sqrt{3} \text{ R30}^{\circ} \text{ Cr}_2\text{O}_3/\text{Ru}(0001)$ rotated honeycomb termination, albeit with notable rotational streaking at all reflexes, which may indicate minor variance in the rotational orientation of the oxide with respect to the underlying Ru(0001) lattice. Careful comparison of the reflex positions in this pattern to those collected from bare Ru(0001) (not shown) is consistent with the formation of a fully relaxed $Cr_2O_3(0001)$ termination (a ≈ 5.0 Å), in agreement with detectable lattice mismatches observed for previous films grown on similar metal single-crystals.2

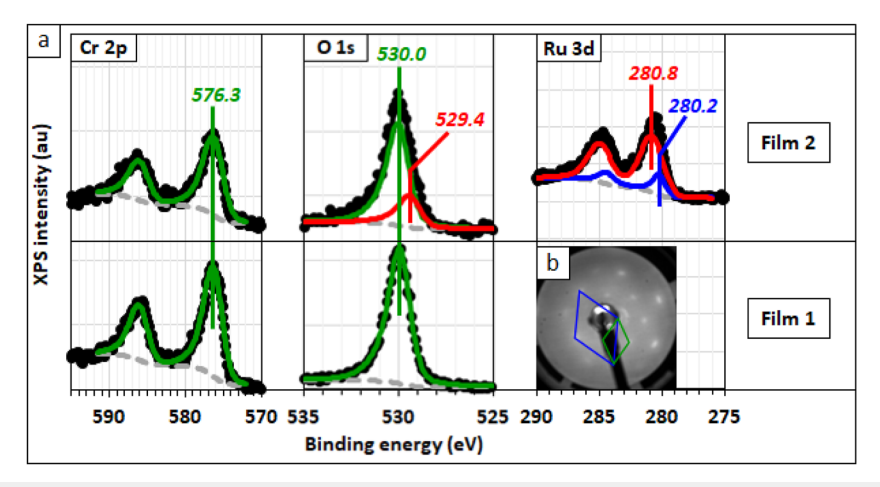


FIG. 1. (a) Cr 2p, O 1s, and Ru 3d XPS spectra collected after growth of two different chromia films on 160 nm Ru(0001)/Al₂O₃(0001). Film 1 (lower spectra) was produced by sequential deposition of ~0.8 nm Cr within Ar, followed by ~8.5 nm CrO_x equivalents of Cr within Ar/O₂ at 350 °C, and subsequent annealing to 700 °C within the Ar/O₂ environment. Film 2 (upper spectra) was produced using an analogous procedure, omitting the intermediate reactive deposition of ~8.5 nm CrO_x. Green fits are attributed to Cr₂O₃, red fits are attributed to RuO₂, and blue fits are attributed to Ru⁰. Peak locations are provided for the Cr 2p_{3/2}, O 1s, and Ru 3d_{5/2} components of each fit. (b) LEED pattern collected from film 2 (E_{e^-} = 100 eV). Superimposed blue and green rhombuses indicate reciprocal lattices associated with Ru(0001) and $\sqrt{3} \times \sqrt{3}$ R30° Cr₂O₃/Ru(0001), respectively.

Figure 2 compares the XPS spectra collected from film 1 to those obtained from a 1.5 nm thick CrO_x film deposited on 160 nm Ru(0001) by 450 °C reactive deposition of Cr within Ar/O₂ (film 3) before and after annealing to 600 °C in the presence of the Ar/O₂ environment. Unlike film 2, Ru is found to remain in its metallic state both before and after the oxidative annealing following this processing sequence. Prior to annealing, several differences emerge when comparing the Cr 2p and O 1s spectra to those collected from film 1. First, the location of both sets of peaks shifts ~0.2 to 0.3 eV toward higher binding energies. Similar collective shifts have been attributed to decreased Ru work-function and minimized repulsive dipole interactions resulting from the loss of Ru-bound O adatoms present at the metallic interface of other oxide/Ru thin-film which is consistent with the absence of oxide contributions to the Ru 3d spectrum. Second, the O 1s:Cr 2p peak ratio decreases from 0.43:1 to 0.35:1, potentially indicating substoichiometric oxidation of the chromia film. To efficiently establish conditions potentially leading to more complete chromia oxidation without the formation of RuO2, a series of in situ NAP-XPS measurements were collected as a function of sample temperature within 0.8 mTorr O2. By monitoring the Cr 2p, O 1s, and Ru 3d peak positions, the film was heated in 50 °C increments until the Cr 2p and O 1s positions and ratio became consistent with those exhibited by film 1, which occurred at 600 °C. For improved self-consistency, the upper plot provided in Fig. 2 provides data collected from this sample within the UHV system used to produce all other XPS figures presented in this work (Cr $2p_{3/2} = 576.3$ eV, O 1s = 530.0 eV, and Cr 2p:O 1s = 0.45:1).

Figures 3(a) and 3(b) provide LEED images collected from film 3 before (a) and after (b) annealing to 600 °C within Ar/O₂. Both clearly indicate the formation of a relaxed Cr₂O₃(0001) surface structure. Unlike Fig. 1(b), reflexes diffracted from these samples are

significantly more circularly symmetric, suggesting improved long-range rotational ordering of the oxide with respect to Ru(0001). Transitioning from Figs. 3(a) and 3(b), the pattern becomes significantly sharper, suggesting further increases to long-range order following $600\,^{\circ}\mathrm{C}$ Ar/O₂.

To more efficiently produce reliably consistent films of varied thickness, the process used to produce film 3 was adapted to consist solely of reactive deposition of varied amounts of Cr within the Ar/O_2 environment at $600\,^{\circ}$ C. XPS spectra collected from such films (not shown) were consistent with those shown after annealing film 3 within Ar/O_2 at $600\,^{\circ}$ C (upper panel in Fig. 2), and self-consistent reciprocal lattices continue to be observed by LEED with increasing chromia thickness. Figure 3(c) provides a pattern collected from 5 nm Cr_2O_3 deposited on 100 nm Ru(0001) via this process. While reflexes become somewhat more diffuse due to presumptive increases in surface charging with increasing chromia thickness, relative locations continue to exhibit six-fold symmetry consistent with a relaxed $Cr_2O_3(0001)$ surface plane.

All $Cr_2O_3/Ru(0001)/Al_2O_3(0001)$ films exhibited 2θ XRD characteristics consistent with those reported previously by our group for Ru(0001) films grown on $Al_2O_3(0001)$ wafers. ⁵⁴ Unfortunately, this includes small peaks of unknown origin at both $2\theta=39.9^{\circ}$ and 86.0° that preclude conclusive disambiguation of diffraction from the (0006) and (00012) planes expected for epitaxial Cr_2O_3 thin-films relative to diffracted intensities collected at the same geometries from uncovered $Ru(0001)/Al_2O_3(0001)$ wafers. XRD data comparing theta-2theta scans collected from $Ru(0001)/Al_2O_3(0001)$ with and without subsequent exposure to deposition conditions expected to result in epitaxial growth of $Cr_2O_3(0001)$ are provided as Fig. S1 within an accompanying supplementary material document. It is important to note that others have previously reported XRD scans

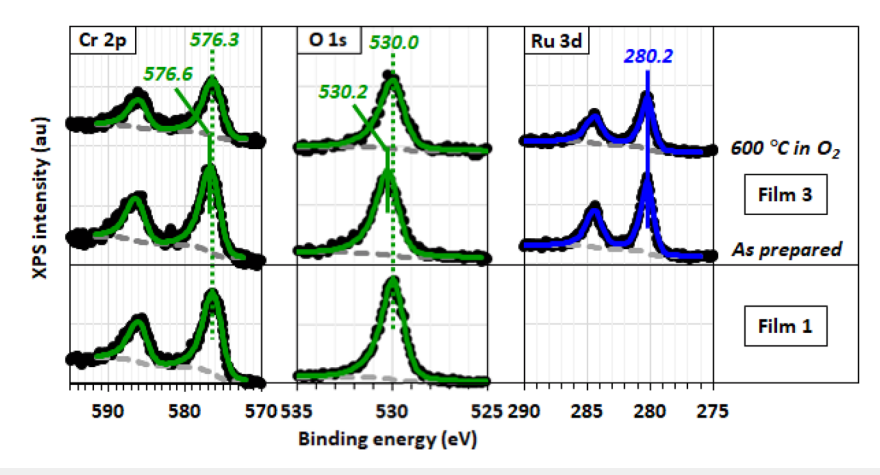


FIG. 2. Cr 2p, O 1s, and Ru 3d XPS spectra collected after growth of 1.5 nm $CrO_x/Ru(0001)$ via reactive deposition of Cr at 450 °C within the Ar/O_2 environment (film 3) both before and after heating to 600 °C within Ar/O_2 (upper plots) are compared to those exhibited by film 1 described in Fig. 1 (lower plot). Green fits are attributed to Cr_2O_3 , and blue fits are attributed to Ru^0 . Peak locations are provided for the $Cr_2O_{3/2}$, O 1s, and $Ru_3O_{5/2}$ components of each fit.

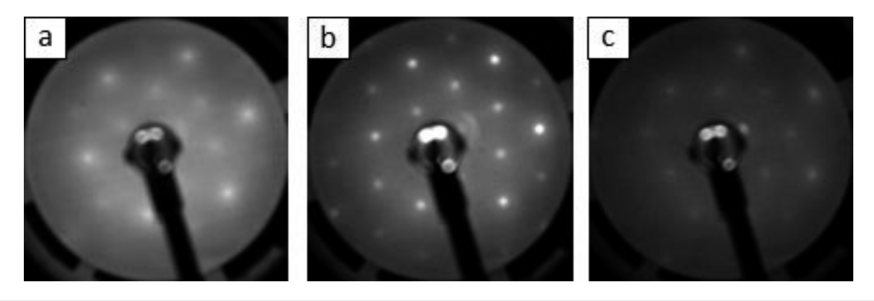


FIG. 3. (a) and (b) LEED patterns collected from film 3 (see Fig. 2) before (a) and after (b) annealing the CrO_x/Ru(0001) film to 600 °C within Ar/O₂. (c) LEED pattern collected from 5 nm Cr₂O₃ produced by reactive deposition of Cr within Ar/O₂ at 600 °C on 100 nm Ru(0001). E_a = 100 eV in all cases.

for Ru(0001) grown on $Al_2O_3(0001)$ devoid of the source of our peak overlap complications when using a monochromatic light source, ⁶¹ but it is unclear the extent to which the observed discrepancy with our results reflects differences in light source characteristics or sample purity.

B. High temperature Cr₂O₃/Ru(0001) film characteristics

Despite ubiquitous application as high-temperature, corrosion-resistant passivation layers, any attempt to heat the $Cr_2O_3/Ru(0001)$ films to temperatures above $400\,^{\circ}C$ within non-oxidative environments leads to rapid film degradation, as evidenced by the near complete loss of Cr from the surface (observed by both XPS and XRR). This effect is observed if heating in UHV, Ar, or Ar/H₂ manifests similarly independent of Cr_2O_3 film thickness (for films ≤ 20 nm). For this reason, all films described above were cooled to room temperature within Ar/O₂ prior to removal from the deposition chamber. Given the robust thermal stability of unsupported chromia, this effect is necessarily attributable to interactions

unique to the $Ru-Cr_2O_3$ interface. Non-mutually exclusive possibilities accounting for these observations include chromia desorption, dewetting, and interlayer mixing. An in-depth analysis needed to fully disambiguate these possibilities was not carried out, but trends indicative of the post-mortem film characteristics are summarized below

Figure 4 depicts changes in XPS spectra noted when heating film 2 (overoxidized 1.5 nm Cr_2O_3) to $600\,^{\circ}C$ within UHV ($\sim 1 \times 10^{-8}$ Torr). UHV typically presents a mildly reducing environment due to disproportionately large background partial pressures of CO and H_2 . Among several noteworthy effects, the most obvious change observed after heating in UHV is the increase in Ru 3d signal intensity coupled with concomitant decreases in Cr 2p and O 1s peak intensities. Quantitative comparison of integrated intensities results in Cr 2p:Ru 3d = 0.45:1 (compared to 2.3:1 for the fully oxidized version of film 3). XRR modeling only provides reliable estimates of film thickness down to a lower limit threshold of ~ 1 nm, but changes in XPS intensities can be modeled to provide thickness estimates for thinner films assumed to adapt CrO_x/Ru layered configurations. 62 Despite providing reasonably accurate esti-

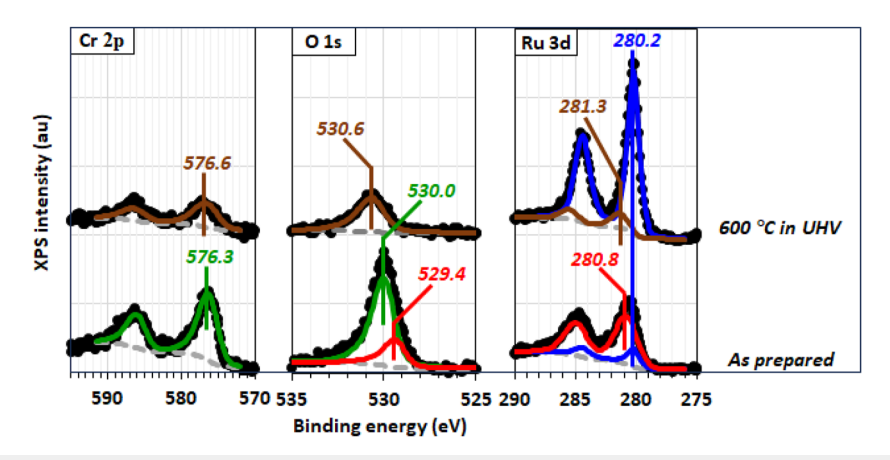


FIG. 4. Cr 2p, O 1s, and Ru 3d XPS spectra collected before (lower plots) and after (upper plots) annealing film 2 (see Fig. 1) to 600 °C within UHV (\sim 1 x 10⁻⁸ Torr). Green fits are attributed to Cr₂O₃, red fits are attributed to RuO₂, blue fits are attributed to RuO₃, and brown fits are attributed to the formation of an ill-defined Ru_xCr_yO_z structure. Peak locations are provided for the Cr 2p_{3/2}, O 1s, and Ru 3d_{5/2} components of each fit.

mates of other Ru-supported oxide films (i.e., SiO_2 and MoN), similar approaches used to model comparative XPS signals collected from $Cr_2O_3/Ru(0001)$ using inelastic electron mean free paths generated by the NIST EAL database appear to systemically overestimate the oxide film thicknesses by $\sim 2.7 \times$ when compared to reliable XRR (and TEM) values. Accounting for this systemic error, the Cr 2p:Ru 3d integrated intensity ratio exhibited by the UHV annealed film is consistent with Ru covered by ~ 4.5 Å Cr_2O_3 , which is roughly equivalent to the height of a primitive $Cr_2O_3(0001)$ unit-cell measured perpendicular to the Ru interface. Equivalent changes in relative XPS intensities could also manifest if heating leads to Ru- Cr_2O_3 interlayer mixing or dewetted chromia island formation.

In addition to the drastic attenuation of chromia features, each of the core-level spectra develops new features at different binding energies, after annealing in UHV (brown fits). Fit as single components, both Cr 2p and O 1s peaks shift several tenths of an eV to higher binding energies and a new shoulder emerges at 281.3 eV within the Ru $3d_{5/2}$ spectrum. Analogous peak components are also present after annealing films that do not exhibit evidence of RuO2 prior to heating (i.e., such as film 3). A direct interpretation accounting for all shifts is not immediately apparent, but their presence suggests significant differences in the nature of the chemical-state of all atoms present within the surviving Ru_xCr_yO_z surface structure relative to those in the bulk of the Cr₂O₃ and Ru films. In addition to changes in peak locations, the O 1s:Cr 2p integrated intensity ratio increases from 0.45:1 to 0.52:1, suggestive of modest stoichiometric enrichment of O relative to Cr within the ill-defined post-annealed surface structure relative to that within the bulk of the as-prepared

Figure 5 shows changes in the LEED pattern that emerge after heating film 2 to 600 °C within UHV. Visual inspection in Fig. 5(b) immediately indicates the presence of a new and very ordered surface structure. Whereas the precursor pattern [Fig. 5(a)] is diffuse and rotationally streaked about the reflexes, the pattern observed after heating is very well resolved without evidence of streaking.

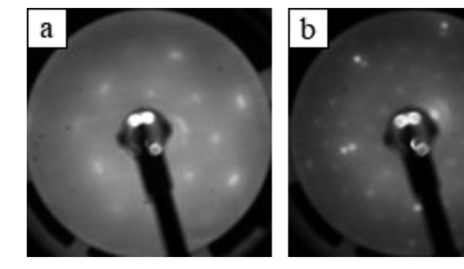


FIG. 5. LEED patterns collected from film 2 (see Fig. 1) before (a) and after (b) annealing to 600 $^{\circ}$ C within UHV. (a) $E_{e^-} = 100$ eV and (b) $E_{e^-} = 77$ eV.

Whereas Ru(0001) reflexes are not unambiguously visualized in patterns collected from the other films, reflexes attributed to the metal substrate are readily distinguished from the remainder of the pattern obtained after heating to 600 °C. Due to the limited sampling depth, the presence of these LEED spots supports the presence of a degradation mechanism leading to the formation of a thin overlayer structure on the Ru(0001) interface. Careful comparison of the reciprocal lattice vectors indicates the formation of a $\sim 3.8 \times 3.8 \text{ R}30^{\circ}$ Ru_xCr_yO_z/Ru(0001) superstructure. The lattice parameter associated with this structure (a \approx 10.3 Å) is not readily attributable to known chromia- or Ru-containing hexagonal surface terminations. Interestingly, the lattice is, however, almost exactly intermediate between those expected for 2×2 reconstructions of $Cr_2O_3(0001)$ (a = $4.9407 \text{ Å})^{6-14}$ and $Ru_2O_3(0001)$ (a = $5.293 \text{ Å}).^{64}$ Further investigation is required to more fully characterize the nature of this structure and its possible scientific applications, which is beyond the scope of

Given the propensity for Cr_2O_3 degradation at temperatures above $400\,^{\circ}C$ within non-oxidative environments and the propensity for Ru oxidation at temperatures above $600\,^{\circ}C$ within mTorr O_2 , attempts were made to establish an environment that might

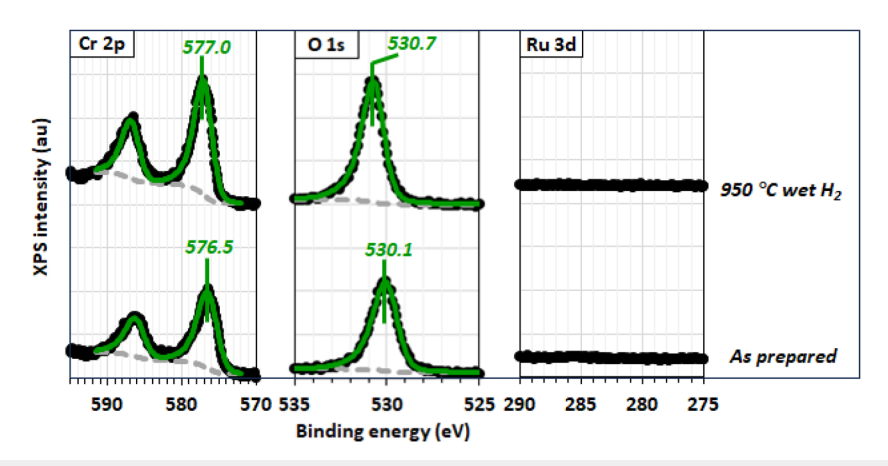


FIG. 6. Cr 2p, O 1s, and Ru 3d XPS spectra collected before (lower plots) and after (upper plots) annealing a \sim 20 nm Cr₂O₃(0001) film grown on \sim 40 nm Ru(0001) to 950 °C for 1 min within 1 atm wet Ar/H₂ 3%. Green fits are attributed to Cr₂O₃. Peak locations are provided for the Cr 2p_{3/2} and O 1s components of each fit.

thermodynamically favor the oxidation of Cr (but not Ru) as a means to potentially stabilize the $\rm Cr_2O_3/Ru(0001)$ films when heated to temperatures above 600 °C. To accomplish this, wafer segments were heated to temperatures as high as 950 °C within a wet hydrogen environment established by bubbling Ar/H $_2$ 3% through water before flowing the gaseous mixture through a freely exhausted quartz tube furnace.

Figure 6 provides XPS spectra collected from a ~20 nm Cr₂O₃ film grown on ~40 nm Ru(0001) by reactive deposition of Cr within Ar/O2 at 600 °C before and after annealing to 950 °C for 1 min within the aforementioned wet hydrogen environment. Prior to annealing, only Cr 2p and O 1s features are detected in the Cr₂O₃ film. Both peaks are shifted ~0.1 to 0.2 eV toward increased binding energies relative to those collected from thinner versions of the film. These shifts are readily attributable to increased charging contributions resulting from the thicker insulating film. A comparison of the O 1s:Cr 2p integrated intensity ratio reveals no significant change in film stoichiometry relative to that of the fully oxidized, thinner variants of the film. The Ru 3d signal remains undetectable after completing the wet hydrogen annealing process, indicating that the change in the gas-phase environment is sufficient to mitigate the catastrophic film degradation effects noted when heating in non-oxidizing conditions. While the film clearly remains on the surface, changes are observed in both the Cr 2p and O 1s spectra after the wet hydrogen annealing. First, the O 1s:Cr 2p intensity ratio shifts from 0.41:1 to 0.38:1, indicating a subtle reduction toward substoichiometric surface concentrations of O. Second, both peaks shift ~0.5 to 0.6 eV to higher binding energies. Possible explanations for these shifts may include changes in the insulating quality of the film and/or further reduction of the underlying Ru interface as a result of the annealing process (see discussion in Fig. 2).

To more quantitatively track changes in film thickness, XRR measurements were made before and after completing the wet annealing process described in the previous set of experiments. Results from these measurements are provided in Fig. 7 for 2θ reflection angles ranging from 0 to 4° . Fitting the fringes of the spectra

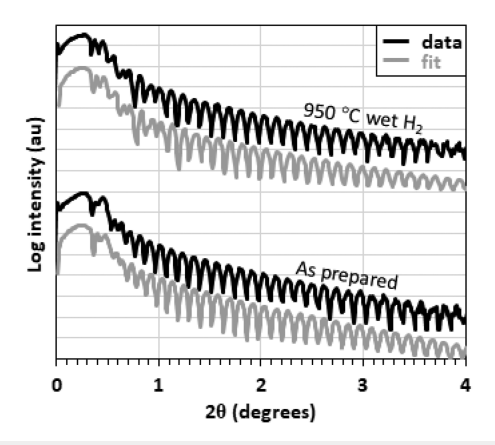


FIG. 7. XRR data and fits associated with a nominally $\sim\!20$ nm $Cr_2O_3(0001)$ film grown on $\sim\!40$ nm Ru(0001) on $Al_2O_3(0001)$ before (lower) and after (upper) annealing to 950 °C for 1 min within 1 atm wet Ar/H₂ 3%.

by genetic algorithm results in the following changes in layer thickness as a function of the annealing process: Cr_2O_3 (24.1 \rightarrow 23.8 nm) and Ru (37.1 \rightarrow 36.8 nm), which both fall near the uncertainty thresholds inherent to the technique. From this, we conclude that $Cr_2O_3/Ru(0001)$ films are stabilized by the wet hydrogen environment when heated to temperatures relevant to the film's disparate sets of potential scientific applications (i.e., calcining refractory active sites and/or high temperature investigations of corrosion within steam environments).

To further investigate the crystallography of thicker $Cr_2O_3(0001)/Ru(0001)$ films, a 20 nm $Cr_2O_3(0001)$ film grown on 20 nm Ru(0001) was, in turn, covered by 20 nm of Ru deposited in Ar at $300\,^{\circ}C$ to potentially seed epitaxial growth of Ru(0001) on the top $Cr_2O_3(0001)$ interface without destroying the Cr_2O_3 layer.

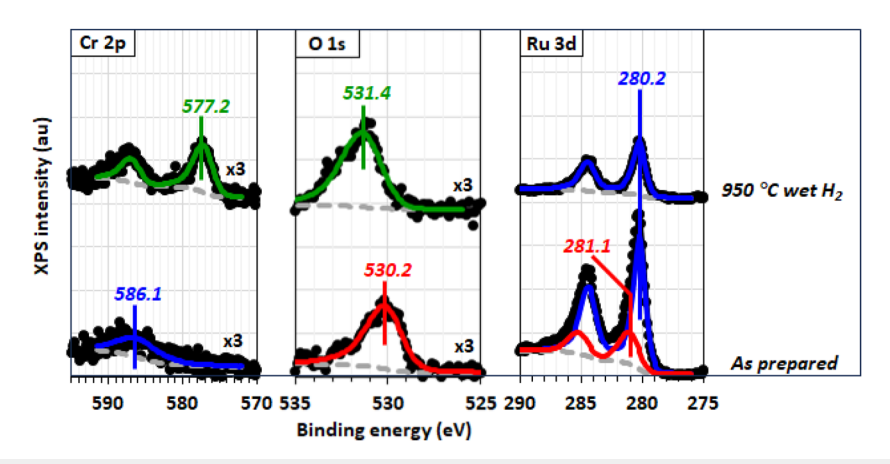


FIG. 8. Cr 2p, O 1s, and Ru 3d XPS spectra collected before (lower plots) and after (upper plots) annealing a \sim 20 nm Ru film deposited at 300 °C in Ar on \sim 20 nm Cr₂O₃(0001) grown on \sim 20 nm Ru(0001) to 950 °C for 1 min within 1 atm wet Ar/H₂ 3%. Intensities in the Cr 2p and O 1s regions have been scaled up by a factor of 3× for clarity. Green fits are attributed to Cr₂O₃, red fits are attributed to O–Ru, and blue fits are attributed to Ru⁰. Peak locations are provided for the Cr 2p_{3/2}, O 1s, and Ru 3d_{5/2} components of each fit.

XPS spectra collected from this sample before and after annealing to 950 °C for 1 min within the wet H₂ environment are provided in Fig. 8. Prior to annealing, only Ru and O species are detected, indicating complete coverage of the underlying Cr₂O₃ layer. Specific features are attributable to metallic Ru (blue) and the presence of chemisorbed O adatoms at the exposed Ru surface (red) (Ru 3d_{5/2} = 281.1 eV and O 1s = 530.2 eV). The small peak present at 586.1 eV is attributed to Ru 3s, which has been omitted from other Cr 2p fits due to its comparably negligible peak intensity when characterizing chromia capped Ru films. Wet H2 annealing of this sample to 950 °C results in significant changes in the XPS spectra. Most notably, the Ru 3d integrated intensity decreases by more than a factor of 3, and Cr 2p is detected, indicating the existence of some mechanism by which Ru coverage of the underlying Cr2O3 layer diminishes during the annealing process. Plausible explanations include dewetting of the Ru layer to expose regions of Cr2O3 or interlayer mixing. Assuming the former (see TEM results below), a few lingering observations must be rationalized. First, both Cr 2p and O 1s now appear at higher binding energies than were observed after wet annealing the uncovered Cr₂O₃ film (Fig. 6). More specifically, the binding energy of Cr 2p increases by ~0.2 eV, while that of O 1s increases by ~0.7 eV. Notably, these shifts agree well with the increases in respective binding energies detected after heating Cr₂O₃ in a vacuum to create the Ru_xCr_yO_z structure described in Figs. 4 and 5. Second, such as the previous post-annealing structure, we again also note increased O concentration relative to that in Cr_2O_3 , albeit significantly more so in this case (O 1s:Cr 2p \rightarrow 0.83). From this, we conclude that the interfacial chromia still undergoes some form of modification resulting from interaction with Ru at elevated temperatures, but that adhesion of the Cr2O3 bulk is somehow better stabilized as a result of the change in atmosphere when heating in the presence of wet hydrogen instead of UHV, Ar, or Ar/H₂.

To better examine the fate of the previous sample, a wet hydrogen annealed segment of the wafer was selected for additional S/TEM characterization. Figure 9(a) is a bright-field (BF) transmission electron microscopy (TEM) image of the heterostack. The agglomeration, i.e., dewetting, of the top Ru layer is evident in the image. The Ru islands are ~40 nm thick, indicating that the nominally 20 nm-thick as-deposited layer of Ru now covers only about one half of the surface of the Cr₂O₃ layer. Figure 9(b) presents a higher magnification high-angle annular dark-field (HAADF) scanning TEM (STEM) image of the outlined section of the stack. Since in HAADF imaging intensity is proportional to approximately the square of the atomic number,65 the planarity of the lower Cr₂O₃ interface in comparison to the roughness of its top interface is clearly shown. Figure 9(c) presents the EDS elemental maps of Al, Cr, and Ru. Although these maps are only a qualitative measure of the elemental concentrations, they clearly show the presence of Cr₂O₃ as the interlayer dielectric present between the two Ru layers. EDS line scans of Al, Cr, and Ru as a function of distance across the heterostack showed no measurable intermixing. Figure 10(a) is the high resolution TEM image of the heterostructure and the substrate. The lattice fringes in the sapphire(0001) substrate evidence its crystallinity, and the nanobeam diffraction pattern (NDP) shown in the inset for this layer confirms the zone axis as sapphire $[11\overline{2}0]$. For the Ru layer deposited directly on sapphire, the $[10\overline{1}0]$ zone axis NDPs shown as an inset in Fig. 10(a) demonstrate the rotated honeycomb orientation of this layer relative to the sapphire substrate. This 30° relative rotation of the Ru layer and the sapphire substrate is in agreement with several prior studies. 66-68 The rotated honeycomb orientation reduces the misfit strain for Ru(0001)/sapphire(0001) to 1.5% compared with the hexagon-on-hexagon misfit of 87.5%. Interestingly, the NDP shown in the inset in Fig. 10(a) for the Ru(0001) island atop the chromia layer shows the zone axis to also be $[10\overline{10}]$. This indicates that the orientation of the dewet-

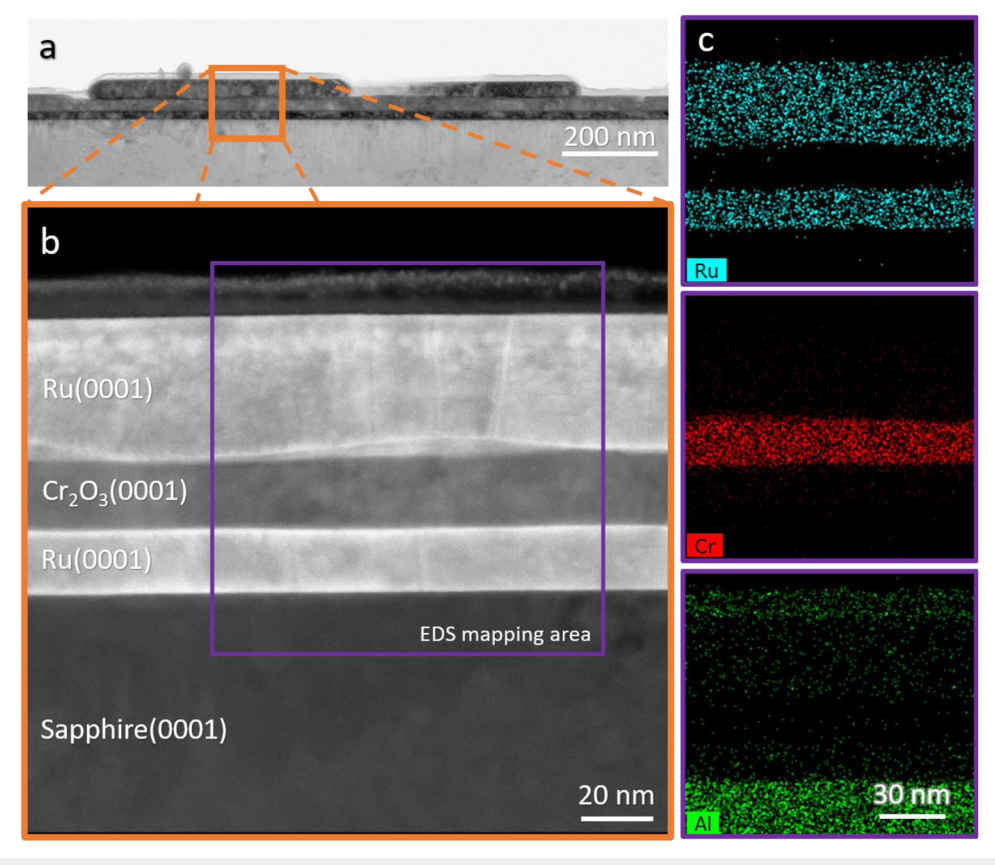


FIG. 9. (a) BF-TEM image of the Ru/Cr₂O₃/Ru/Sapphire(0001) heterostructure showing dewetting of the top Ru layer upon annealing 1 min at 950 °C in a H_2-H_2 O ambient. (b) HAADF STEM image of the section of the stack in the left Ru island in (a) evidencing the planarity of the lower Cr_2O_3 interface in contrast to the roughness of its top interface. (c) EDS elemental maps of Ru, Cr, and Al demonstrating the clear presence of the distinct layers in the sample stack. The aluminum and sputtered aluminum oxide layer deposited as a means of preserving the top of the sample stack are clearly seen in (a) and (b), and in the Al elemental map in (c).

ted Ru layer relative to the sapphire substrate is the same as that for the Ru(0001) layer directly deposited on the sapphire(0001) substrate.

The Cr_2O_3 layer in Fig. 10(a) shows a prominent Moiré contrast, the origin of which will be discussed shortly. Chromium oxide is trigonal, with the same space group $(R\overline{3}c)$ and crystal structure (corundum) as sapphire. However, unlike for the sapphire substrate, the NDP for this layer, shown as an inset, is clearly not a single zone axis pattern. Given that Ru is hexagonal (space group $P6_3/mmc$), the formation of chromia rotational domains may be expected. The basal plane lattice parameter of Ru is $a_{Ru} = 2.7059$ Å. The basal plane lattice parameter of Cr_2O_3 referenced to a hexagonal frame and computed from the reported rhombohedral lattice parameters is $a_{chromia} = 4.9407$ Å. $^{6-14}$ The hexagon-on-hexagon misfit strain for Cr_2O_3 deposited on Ru(0001)/sapphire(0001), calculated as $(a_{Ru} - a_{chromia})/a_{chromia}$, is -45.6%(-44.4%) if Ru is fully relaxed (fully strained). By contrast, if Cr_2O_3 adopts the rotated honeycomb orientation relative to the Ru(0001) layer, then the misfit strain is given by

$$\varepsilon_m = \frac{d_{10\bar{1}0}^{\text{Ru}} - d_{11\bar{2}0}^{chromia}}{d_{11\bar{2}0}^{chromia}} = -5.7\%(-3.7\%),\tag{1}$$

where d's are the interplanar spacings of the given planes in the given material. As can be seen, the magnitude of these compressive misfit strains for the 30° rotated honeycomb orientation for chromia deposited on fully relaxed (fully strained) Ru is significantly lower than for the hexagon-on-hexagon orientation. Therefore, chromia is expected to adopt the rotated honeycomb $Cr_2O_3(0001)$ orientation when forming on Ru(0001), consistent with the LEED pattern interpretations described above.

The NDP of the $Cr_2O_3(0001)$ layer is a superposition of two distinct $\langle 11\bar{2}0 \rangle$ type zone axis patterns, which for concreteness will be taken as $[11\bar{2}0]$ and $[2\bar{1}\bar{1}0]$. Each of these zone axes, and hence, the associated Cr_2O_3 rotational domain, is 30° rotated about the caxis relative to the Ru layer, whose zone axis is $[10\bar{1}0]$. One chromia domain is rotated clockwise, and the other domain is rotated counterclockwise relative to Ru. The superposition of the two zone axis

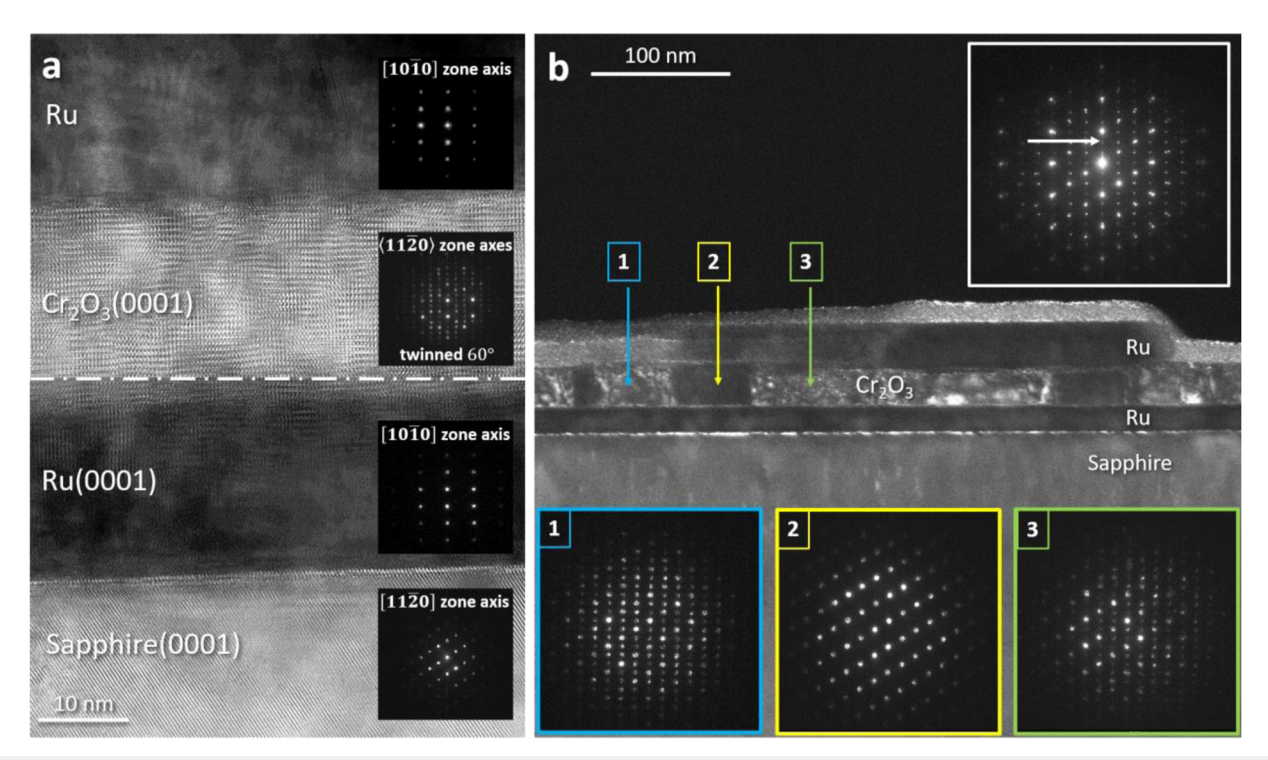


FIG. 10. (a) Two high resolution TEM images of the heterostructure combined at the dotted-dashed line to clearly show all layers of the sample. The insets are nanobeam diffraction patterns (NDP) from the respective layers. (b) Dark-field (DF) TEM image of the heterostructure, with the selected area diffraction pattern of the full stack plus substrate shown in the white-bordered inset (top-right). The DF image was formed with the (0004) beam marked with the white arrow in the inset. This is a forbidden reflection in sapphire, Ru, and Cr_2O_3 and forms as a result of double diffraction. The DF image allows different regions within the Cr_2O_3 layer to be identified for subsequent nanobeam diffraction, shown in three separate insets below the image. Regions marked 1 and 3 show mixed light-dark contrast in the image. They are bicrystalline Cr_2O_3 . Their nanobeam diffraction patterns evidence double diffraction in addition to the superposition of the two mirrored $(11\bar{2}0)$ zone axis patterns for the two variants. The region of dark contrast in the image marked 2 is a single crystalline Cr_2O_3 through the thickness, with a single $[11\bar{2}0]$ zone axis pattern labeled 2 in the inset.

patterns means that both rotational domains are present through the thickness of the electron transparent cross section, thereby also giving rise to the Moiré contrast shown in the high-resolution image of this layer in Fig. 10(a).

Given that electron diffraction in the TEM is dynamical rather than kinematical, a given diffracted beam can act as the incident beam for diffraction from a second or more set of planes (i.e., double diffraction) and result in the appearance of forbidden reflections. The forbidden reflections in the NDP pattern of the Cr₂O₃(0001) layer in Fig. 10(a) are the additional spots that are present above and beyond the superposition of the two $[11\overline{2}0]$ and $[2\overline{11}0]$ zone axis patterns. To generate the forbidden reflection resulting from double diffraction, the zone axis pattern is displaced by placing the direct beam, i.e., \boldsymbol{g}_{0000} , onto an allowed diffraction spot. 71 For concreteness in the NDP in Fig. 10(a), if double diffraction is assumed to occur in the domain with $[2\overline{110}]$ as its zone axis, then placing the origin of the zone axis pattern of the $[11\overline{2}0]$ oriented domain on $\mathbf{g}_{0\overline{1}12}$ and then also on $g_{01\overline{1}4}$ of the $[2\overline{11}0]$ domain will account for all the forbidden reflections shown in the NDP pattern of the Cr₂O₃(0001) layer in Fig. 10(a).

In Fig. 10(b), dark field imaging using an objective aperture at the position of the forbidden reflection g_{0004} , marked with a white arrow in the inset in the top right, shows lateral regions that are either of dark contrast (labeled 2) or of mixed contrast (labeled 1 and 3). NDP patterns collected in each of these three regions then clearly show that in region 2, only a single $[11\bar{2}0]$ Cr₂O₃ domain is present through the electron transparent section, whereas in regions 1 and 3, both rotational domains are present through thickness and result in NDP patterns similar to the pattern shown in Fig. 10(a). The NDPs in Fig. 10(b) again confirm that the epitaxially grown Cr₂O₃(0001) is bicrystalline, with both rotational domains present in the film, but that in select regions of the sample, it is possible to demonstrate the presence of only a single domain.

IV. CONCLUSIONS

A full summary correlating reported film characteristics to various deposition and processing conditions explored in this work is included as Table S1 within the supplementary material accompanying this article. Conditions suitable for the creation of a robust

Cr₂O₃(0001)/Ru(0001) epitaxial thin-film system allowing for versatile structure-property investigations pertinent to wide-ranging disparate fields of study are outlined by this work. Wafer scale deposition of epitaxial Cr₂O₃(0001) bicrystals on sapphire(0001)supported Ru(0001) films has been achieved via reactive sputter deposition of Cr within 4 mTorr Ar/O2 20%. Highly ordered films are produced when heating the wafer to 450-600 °C during deposition, subsequently heating to 600 °C within the oxygen containing atmosphere (for depositions completed below 600 °C), and allowing the wafer to cool to room temperature before evacuating the gas composition from the chamber. The adsorbed films adopt a 30° rotated honeycomb configuration relative to the Ru(0001) substrate and exhibit basal plane lattice parameters consistent with bulk Cr₂O₃(0001). Neglecting charging effects, Cr₂O₃ film characteristics remain self-consistent independent of thickness within the range of depths explored (~1.5-20 nm) when deposited at 600 °C. Heating films at, or above, 700 °C within the O2 environment leads to Ru layer oxidation. By contrast, heating films to temperatures at, or above, 400 °C in 4 mTorr Ar, Ar/H₂ 3%, or vacuum results in film deterioration and the emergence of an incommensurately well-ordered hexagonal Ru_xCr_vO_z surface structure rotated by 30° relative to Ru(0001) with a lattice parameter $a \approx 10.3 \text{ Å}$. Heating $Cr_2O_3(0001)/Ru(0001)$ films in 1 atm flowing wet Ar/H₂ 3% allows for temperatures of at least 950 °C without loss of Cr2O3, Ru oxidation, or evidence of interlayer mixing. Nonetheless, Cr2O3-Ru interactions still appear to similarly affect the nature of surface-bound chromia at elevated temperatures, even when the bulk Cr2O3 film is retained after heating in wet H₂. Ru-Cr₂O₃-Ru heterostacks created by deposition of Ru on Cr₂O₃(0001)/Ru(0001) films within 4 mTorr Ar at 300 °C lead to the formation of dewetted Ru crystals oriented in epitaxial registry with bottom layer Ru(0001) when heated to 950 °C within the wet H₂ environment.

SUPPLEMENTARY MATERIAL

A supplementary material document is included with this article to provide a direct comparison of XRD data taken from $Ru/Al_2O_3(0001)$ samples before and after growth of the $Cr_2O_3(0001)$ film using the recipe established in this work (Fig. S1) and a summary table correlating all film processing conditions and reported outcomes (Table S1).

ACKNOWLEDGMENTS

The funding support from the Air Force Office of Scientific Research, the AFOSR FA9550-22-1-0312 MURI program, and FA9550-22-1-0219 is gratefully acknowledged. E. Yi is thanked for the preparation of the electron transparent section. This work was carried out in part in the Electron Microscopy Laboratory of Columbia Nano Initiative (CNI) Shared Lab Facilities at Columbia University. This work was also supported in part by NSF Grant No. 2018319 and the Materials Characterization Shared Use Facility at the University of Central Florida.

AUTHOR DECLARATIONS

Conflict of Interest

The authors have no conflicts to disclose.

Author Contributions

Quintin Cumston: Conceptualization (supporting); Data curation (equal); Formal analysis (equal); Methodology (equal); Visualization (equal); Writing - review & editing (equal). Matthew Patrick: Data curation (equal); Formal analysis (supporting); Methodology (supporting); Writing - review & editing (supporting). Ahmed R. Hegazy: Data curation (equal); Formal analysis (supporting); Visualization (supporting); Writing - review & editing (supporting). Amirali Zangiabadi: Data curation (equal); Formal analysis (equal); Methodology (equal); Resources (equal); Writing - review & editing (equal). Maximillian Daughtry: Conceptualization (supporting); Data curation (supporting); Methodology (supporting); Writing - review & editing (supporting). Kevin R. Coffey: Conceptualization (equal); Funding acquisition (supporting); Methodology (equal); Project administration (equal); Resources (equal); Supervision (equal); Visualization (equal); Writing - original draft (equal); Writing - review & editing (equal). Katayun Barmak: Conceptualization (equal); Formal analysis (equal); Funding acquisition (lead); Methodology (equal); Project administration (equal); Resources (equal); Supervision (equal); Visualization (equal); Writing - original draft (equal); Writing - review & editing (equal). William E. Kaden: Conceptualization (equal); Formal analysis (equal); Funding acquisition (equal); Methodology (equal); Project administration (equal); Resources (equal); Supervision (equal); Visualization (equal); Writing - original draft (equal); Writing - review & editing (equal).

DATA AVAILABILITY

The data that support the findings of this study are available from the corresponding author upon reasonable request.

REFERENCES

- ¹ A. S. Kilian et al., CrystEngComm 16, 9291 (2014).
- ² A. Pancotti et al., Top. Catal. **54**, 90 (2011).
- ³A. V. Almaev et al., Superlattices Microstruct. **151**, 106835 (2021).
- ⁴R. Auguste et al., npj Mater. Degrad. **6**, 61 (2022).
- ⁵S. Ghotekar et al., Case Stud. Chem. Environ. Eng. 3, 100089 (2021).
- ⁶ A. Vaitkus et al., J. Cheminf. 15, 123 (2023).
- ⁷A. Merkys et al., J. Cheminf. **15**, 25 (2023).
- ⁸ A. Vaitkus, A. Merkys, and S. Grazulis, J. Appl. Crystallogr. 54, 661 (2021).
- ⁹M. Quirós et al., J. Cheminf. **10**, 23 (2018).
- ¹⁰ A. Merkys *et al.*, J. Appl. Crystallogr. **49**, 292 (2016).
- ¹¹S. Grazulis et al., J. Appl. Crystallogr. **48**, 85 (2015).
- ¹²S. Gražulis *et al.*, Nucleic Acids Res. **40**, D420 (2011).
- ¹³S. Grazulis et al., J. Appl. Crystallogr. **42**, 726 (2009).
- ¹⁴R. T. Downs and M. Hall-Wallace, Am. Mineral. **88**, 247 (2003), https://pubs.geoscienceworld.org/msa/ammin/article-abstract/88/1/247/43886/The-American -Mineralogist-crystal-structure.
- ¹⁵A. Jain et al., APL Mater. 1, 011002 (2013).

- ¹⁶S. P. Ong et al., Comput. Mater. Sci. **68**, 314 (2013).
- ¹⁷H. C. Graham and H. H. Davis, J. Am. Ceram. Soc. **54**, 89 (1971).
- ¹⁸K.-C. Wang et al., J. Am. Ceram. Soc. **43**, 509 (1960).
- ¹⁹Y. W. Kim and G. R. Belton, Metall. Trans. 5, 1811 (1974).
- ²⁰ A. Yamauchi, K. Kurokawa, and H. Takahashi, Oxid. Met. **59**, 517 (2003).
- ²¹ D. J. Young and B. A. Pint, Oxid. Met. **66**, 137 (2006).
- ²²K. Wei et al., Corros. Sci. 225, 111587 (2023).
- ²³G. Pacchioni and H. Freund, Chem. Rev. 113, 4035 (2013).
- ²⁴S. Lee et al., J. Am. Chem. Soc. **126**, 5682 (2004).
- ²⁵ A. Sánchez et al., J. Phys. Chem. A **103**, 9573 (1999).
- ²⁶C. Harding et al., J. Am. Chem. Soc. **131**, 538 (2009).
- ²⁷Y. Shen et al., ChemCatChem 11, 5439 (2019).
- 28 C. Xu et al., Phys. Rev. Lett. 67, 3551 (1991).
- ²⁹ F. Rohr *et al.*, Surf. Sci. **372**, L291 (1997).
- 30 C. Xu et al., Surf. Sci. 258, 23 (1991).
- ³¹ M. Bender et al., J. Phys.: Condens. Matter 7, 5289 (1995).
- 32 H. Kuhlenbeck et al., Ber. Bunsenges. Phys. Chem. 96, 15 (1992).
- ³³C. A. Ventrice et al., Phys. Rev. B **46**, 12892 (1992).
- ³⁴H. J. Freund, H. Kuhlenbeck, and V. Staemmler, Rep. Prog. Phys. 59, 283
- 35 S. Ekelund and C. Leygraf, Surf. Sci. 40, 179 (1973).
- ³⁶P. Michel and C. Jardin, Surf. Sci. **36**, 478 (1973).
- ³⁷G. Gewinner et al., Surf. Sci. 78, 439 (1978).
- ³⁸ A. Stierle and H. Zabel, Europhys. Lett. **37**, 365 (1997).
- ³⁹ A. Kramer *et al.*, J. Phys.: Condens. Matter **30**, 074002 (2018).
- ⁴⁰V. Maurice, S. Cadot, and P. Marcus, Surf. Sci. **458**, 195 (2000).
- ⁴¹ M. Bender, I. N. Yakovkin, and H. J. Freund, Surf. Sci. **365**, 394 (1996).
- ⁴²M. Lübbe and W. Moritz, J. Phys.: Condens. Matter **21**, 134010 (2009).
- 43 T. Gloege et al., Surf. Sci. 441, L917 (1999).
- 44X. Wende et al., J. Phys.: Condens. Matter 15, 1155 (2003).
- 45 L. Zhang, M. Kuhn, and U. Diebold, J. Vac. Sci. Technol. A 15, 1576 (1997).
- ⁴⁶W. A. A. Priyantha and G. D. Waddill, Surf. Sci. 578, 149 (2005).

- ⁴⁷C. P. Huggins and R. M. Nix, Surf. Sci. **594**, 163 (2005).
- 48 A. Maetaki et al., Surf. Sci. 445, 80 (2000).
- ⁴⁹ A. Maetaki and K. Kishi, Surf. Sci. **411**, 35 (1998).
- ⁵⁰D. Guo et al., J. Phys. Chem. B **109**, 20968 (2005).
- ⁵¹S. A. Chambers, Surf. Sci. Rep. **39**, 105 (2000).
- 52 Y. Cao, Chemistry (University of North Texas, 2015), p. 37.
- ⁵³ J. W. Arblaster, Platinum Met. Rev. 57, 127 (2013).
- ⁵⁴S. S. Ezzat et al., J. Vac. Sci. Technol. A **37**, 031516 (2019).
- ⁵⁵A. S. Kilian et al., J. Phys. Chem. C 118, 20452 (2014).
- ⁵⁶P. Hones, M. Diserens, and F. Lévy, Surf. Coat. Technol. 120-121, 277 (1999).
- 57 J. F. Moulder et al., Handbook of X-Ray Photoelectron Spectroscopy (Perkin-Elmer Corporation, Eden Prairie, Minnesota, 1992).
- ⁵⁸ J.-Q. Zhong et al., J. Phys. Chem. C **123**, 13578 (2019).
- ⁵⁹W. E. Kaden *et al.*, Phys. Rev. B **89**, 115436 (2014).
- 60 A. Khaniya et al., Surf. Sci. Spectra 27, 024009 (2020).
- ⁶¹ S. Kurdi *et al.*, J. Appl. Phys. **127**, 165302 (2020).
- ⁶² A. Khaniya and W. E. Kaden, Top. Catal. **62**, 1035 (2019).
- 63 C. J. Powell and A. Jablonski, NIST Electron Effective-Attenuation-Length Database (National Institute of Standards and Technology, MD, 2011) Version
- ⁶⁴M. E. Grillo, Phys. Rev. B **70**, 184115 (2004).
- $^{\bf 65}{\rm N.}$ Tanaka, Scanning Transmission Electron Microscopy of Nanomaterials: Basics of Imaging and Analysis (Imperial College Press, 2014).
- 66 E. Milosevic et al., J. Appl. Phys. 124, 165105 (2018).
- 67 S. Yamada et al., Jpn. J. Appl. Phys. 41, L206 (2002).
- 68 K. Barmak et al., J. Appl. Phys. 128, 045304 (2020).
- ⁶⁹E. R. Dobrovinskaya, L. A. Lytvynov, and V. Pischik, Sapphire: Material, Manufacturing, Applications (Springer, 2009), p. 158.
- ⁷⁰ M. Grundmann, Phys. Status Solidi B **248**, 805 (2011).
- ⁷¹P. B. Hirsch et al., Electron Microscopy of Thin Crystals, 1st ed. (Butterworth/Heinemann, 1965).